remote sensing

MDPI

Article

Near-Bottom ROV-Borne Self-Potential Exploration of Seafloor Massive Sulfide Deposits on the Southwest Indian Ridge

Zuofu Nie [1,2], Chunhui Tao [1,2,*], Zhongmin Zhu [2,3] and Jianping Zhou [2]

[1] School of Oceanography, Shanghai Jiao Tong University, Shanghai 200030, China; 1454685400@sjtu.edu.cn
[2] State Key Laboratory of Submarine Geosciences and Demarcation, Second Institute of Oceanography, Ministry of Natural Resources, Hangzhou 310012, China; zhuzm@sio.org.cn (Z.Z.); zhoujp@sio.org.cn (J.Z.)
[3] Hubei Key Laboratory of Marine Electromagnetic Detection and Control, Wuhan Second Ship Design and Research Institute, Wuhan 430205, China
* Correspondence: taochunhuimail@163.com

Highlights

What are the main findings?

- Near-bottom ROV-borne SP exploration resolves fine-scale current density anomalies associated with seafloor massive sulfide mineralization in a large, topographically complex hydrothermal field.
- The 3D current density model refines anomaly zones previously identified by AUV-based and towed SP surveys and reveals a segmented distribution of sulfide-related current sources, with primary anomalies supported by visual observations and drilling evidence and secondary anomalies indicating additional potential mineralization.

What are the implications of the main findings?

- The integration of ROV-borne SP data with adaptive octree meshing provides a practical and computationally efficient framework for large-scale imaging of SMS systems in complex seafloor environments.
- ROV-borne near-bottom SP measurements enhance the detectability of weak and localized anomalies, offering improved constraints on the spatial distribution of sulfide mineralization.

Abstract

Seafloor massive sulfide (SMS) deposits formed by hydrothermal circulation generate measurable self-potential (SP) anomalies in seawater, providing an effective geophysical indicator of sulfide mineralization. In this study, a remotely operated vehicle (ROV)-borne SP survey was conducted at the Yuhuang hydrothermal field on the Southwest Indian Ridge to investigate the spatial distribution of SMS mineralization. The survey operated at a near-bottom altitude of approximately 10 m, substantially lower than that typically achieved by autonomous underwater vehicles (AUVs) or towed systems, enabling high-resolution data acquisition with improved signal quality. To efficiently discretize complex seafloor topography under irregular data coverage, an adaptive octree mesh was employed, enabling computationally efficient three-dimensional inversion over a large survey area and recovery of the subsurface source current density distribution. The inversion results resolve a main anomaly zone spatially correlated with known SMS mineralization, as well as an additional anomaly zone that was not resolved by previous surveys and suggests potential mineralization. Anomalies associated with known mineralization show good spatial agreement with independent near-bottom observations and drilling results. The results demonstrate that ROV-borne SP surveying combined with adaptive meshing and

Check for updates

Academic Editor: Chung-yen Kuo

Received: 27 February 2026
Revised: 28 March 2026
Accepted: 1 April 2026
Published: 3 April 2026

Copyright: © 2026 by the authors. Licensee MDPI, Basel, Switzerland. This article is an open access article distributed under the terms and conditions of the Creative Commons Attribution (CC BY) license.

three-dimensional inversion provides a reliable approach for imaging SMS mineralization in deep-sea environments.

Keywords: 3D geophysical imaging; source current density; octree meshing; marine mineral exploration; Yuhuang hydrothermal field

1. Introduction

Seafloor massive sulfide (SMS) deposits formed by hydrothermal circulation represent an important marine mineral resource and play a key role in oceanic geochemical cycles [1]. These SMS deposits are commonly associated with focused fluid discharge, subseafloor permeability contrasts, and intense water-rock interaction at mid-ocean ridges [2]. Accurate delineation of SMS deposits hidden beneath the seafloor remains a major challenge due to the limited accessibility of deep-sea environments and the strong influence of complex bathymetry. Conventional near-bottom visual observations primarily document exposed sulfide occurrences at the seafloor and provide little constraint on buried mineralization, while drilling operations are costly, logistically demanding, and typically limited in penetration depth, particularly in rugged hydrothermal terrains [3–5]. As a result, geophysical methods capable of imaging subsurface structures are required to support the exploration and assessment of SMS deposits.

The self-potential (SP) method has been widely used in terrestrial mineral exploration and resource evaluation, because mineralization-related fluid flow and redox processes generate measurable natural electric fields [6–9]. Xie et al. (2023) have systematically summarized the theoretical basis, numerical modeling, and inversion strategies, highlighting its effectiveness for ore prospecting [10]. In marine settings, SP anomalies produced by SMS deposits can be detected in the surrounding seawater, providing a passive and non-invasive geophysical tool for identifying active venting and associated sulfide mineralization [11,12].

Marine SP measurements are typically conducted in the water column using non-polarizable electrodes to record the potential difference between the pair of electrodes. SP anomalies associated with seafloor hydrothermal systems are commonly characterized by localized negative or dipolar signals with amplitudes ranging from several to tens of millivolts [13–16]. To date, numerous marine SP surveys using a variety of platforms have been conducted in hydrothermal fields to locate hydrothermal activities and SMS deposits. For example, Kawada et al. (2017) used a deep-towed electrode array system, which has six electrodes mounted on an elastic rod, highlighting the effectiveness of specialized deep-sea SP instrumentation for hydrothermal ore exploration [13]. Zhu et al. (2020) deployed a custom-designed electrode array mounted on a double-towed transient electromagnetic system at the Yuhuang hydrothermal field, with the electrodes installed on the relay cable between the two towed bodies, which reduced electrode swinging during towing and ensured more stable measurements [14]. Towed systems enable fast regional-scale reconnaissance but generally operate at relatively high and variable altitudes above the seafloor, resulting in reduced spatial resolution and limited sensitivity to small or shallow sulfide bodies.

Over the past decade, AUV-based SP surveys have been implemented and evaluated in the field, offering superior navigation accuracy and finely controlled survey attitude compared to conventional towed systems [17–23]. For example, Constable et al. (2018) demonstrated that AUV-based SP measurements could resolve fine-scale SP variations at seafloor hydrothermal sites, providing insights into subsurface fluid pathways and localized sulfide accumulation [19]. Similarly, Su et al. (2022) deployed a SP measurement

system on the tail of the AUV and imaged the geometry of SMS deposits beneath the seafloor [20]. Szitkar et al. (2021) developed a passive electric field sensor system mounted on an AUV and combined it with magnetic measurements at the TAG hydrothermal field, highlighting the value of multi-physics approaches in distinguishing active and inactive SMS deposits [22]. These studies demonstrate that AUV-SP surveys are a reliable and non-invasive tool for the characterization of SMS deposits.

In addition, integrating geophysical instruments with remotely operated vehicles (ROVs) allows surveys to be conducted at much lower and precisely controlled near-bottom altitudes (typically on the order of 2–10 m), thereby improving signal fidelity and sensitivity to small-scale anomalies, albeit at relatively low operational speeds (~0.4–1.0 kn). Studies have demonstrated that ROV-based geophysical surveys can achieve high-resolution mapping of hydrothermal systems under complex seafloor conditions, with positioning accuracy of ~1 m and stable attitude control during data acquisition [24,25].

Quantitative inversion of marine SP data is crucial to the evaluation of SMS deposits. SP anomalies caused by mineral deposits, which are heavily related to redox reactions, are interpreted in terms of dipolar source distributions [26]. Revil et al. (2001) introduced a tomographic approach to SP interpretation that images the spatial distribution of electrochemical source current density from surface SP data, providing a physically based framework for quantitative SP inversion [27]. To support accurate forward modeling in marine environments, a three-dimensional analytical solution was derived for the self-potential field generated by regularly polarized bodies in a layered seafloor model, serving as a benchmark for quantitative inversion of marine SP data [28]. In marine settings, SP inversion techniques were applied to SP data over hydrothermal fields, allowing quantitative imaging of subsurface sulfide deposits [14,20]. For example, Kawada et al. (2018) revealed the subsurface source current density distribution associated with the Sunrise SMS deposit, demonstrating that SP inversion can resolve both the geometry and intensity of sulfide mineralization along the Izu–Ogasawara arc in southern Japan [18]. Subsequently, multi-component SP data have been combined with tomographic inversion to further improve the accuracy of subsurface source current density reconstruction [21]. Collectively, these advances demonstrate that SP inversion, when integrated with advanced near-bottom platforms, provides a powerful, non-invasive tool for characterizing SMS deposits and guiding mineral exploration in hydrothermal environments.

Conventional discretization methods are efficient and well suited for relatively simple geological settings, such as flat seafloor conditions, small-scale surveys, or preliminary interpretation. However, the processing of marine SP data acquired from near-bottom ROV surveys can pose computational challenges for 3D inversion. The very low and variable survey altitude results in large volumes of sampled data over extensive areas, while the presence of rugged seafloor topography introduces strong geometric complexity into the forward and inverse modeling. Applying uniform discretization schemes to such datasets often leads to prohibitively high computational cost and memory requirements, particularly when large-scale inversion domains are required. Adaptive octree meshes provide an effective solution by enabling fine discretization in regions of interest, such as near the seafloor and data-dense areas, while maintaining coarser resolution elsewhere to reduce the overall number of model parameters [29,30]. This approach significantly improves computational efficiency without compromising the resolution required to image shallow subsurface features. When integrated with three-dimensional SP inversion, adaptive octree meshing balances computational efficiency with inversion accuracy by adaptively refining the mesh at key locations—thereby facilitating the recovery of source current density distributions that represent subsurface hydrothermal activity and associated sulfide mineralization.

In this study, we present an ROV-based SP survey conducted at the Yuhuang hydrothermal field on the Southwest Indian Ridge (Figure 1). By integrating near-bottom SP measurements with adaptive octree meshing and large-area three-dimensional inversion, we aim to image the subsurface source current density distribution and delineate sulfide-bearing zones beneath the seafloor.

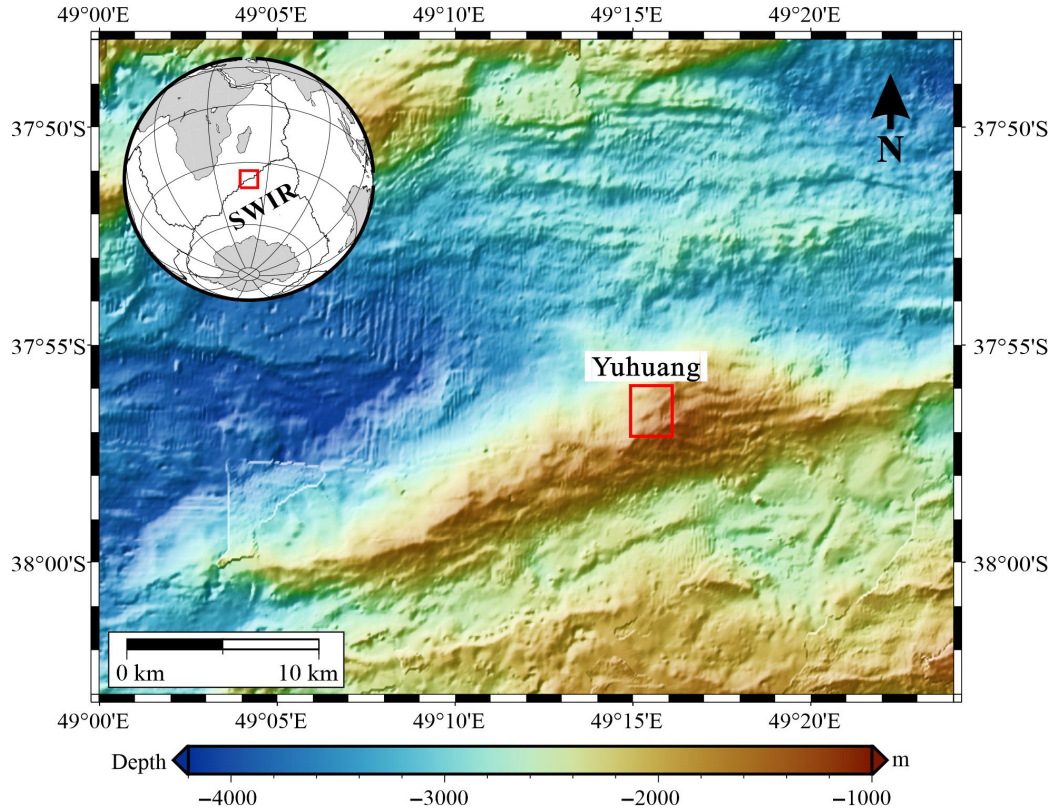

Figure 1. Bathymetry map showing the location of the Yuhuang hydrothermal field (indicated by red square) at SWIR.

2. Methods

2.1. SP Forward and Inverse Problems

Under quasi-static conditions, electric charge conservation requires that

$$\nabla \cdot \mathbf{J} = 0, \tag{1}$$

where the total current density $\mathbf{J}$ is given by

$$\mathbf{J} = -\sigma \nabla \phi + \mathbf{J}_s. \tag{2}$$

Here, ϕ denotes the electric potential, σ is the electrical conductivity distribution, and $\mathbf{J}_s$ represents the source current density describing electrokinetic and electrochemical processes related to mineralization.

Substituting Equation (2) into Equation (1) yields the governing equation for SP fields [8,31]:

$$\nabla \cdot (\sigma \nabla \phi) = \nabla \cdot \mathbf{J}_s. \tag{3}$$

For numerical implementation, Equation (3) is discretized using a finite-volume formulation on a three-dimensional mesh, resulting in Equation (4):

$$\mathbf{D\Sigma G\phi} = \mathbf{DJ}_s, \tag{4}$$

where **G** and **D** denote the discrete gradient and divergence operators, respectively, **Σ** is a diagonal matrix of face-centered electrical conductivities, and **ϕ** is the vector of cell-centered electric potentials [32,33]. To accurately and efficiently simulate the SP field in complex 3D geological settings, we employ an adaptive octree mesh using the TreeMesh module in the SimPEG framework (version 0.20.0), implemented in Python 3.9.12 [29]. This approach reduces the total number of unknowns and computational cost without sacrificing solution accuracy [30,34,35] (Figure 2a). The fundamental principle of octree mesh is to recursively subdivide the entire 3D domain into eight smaller cubic regions, called octants, thereby forming a tree-like hierarchy (Figure 2b). Refinement is applied based on user-specified criteria (e.g., proximity to sources or features of interest) and continues until the target resolution is met or the maximum tree depth is reached. As shown in Figure 2c, the parameters on the octree mesh are defined as follows: current densities $\mathbf{J}_s$ are assigned to the cell faces, whereas electric potentials **ϕ** and conductivities **σ** are defined at the cell centers. The conductivity values at the faces can be calculated by averaging the conductivities of the adjacent cell centers. This arrangement ensures accurate flux evaluation across cell boundaries and maintains consistency between potential and current representations.

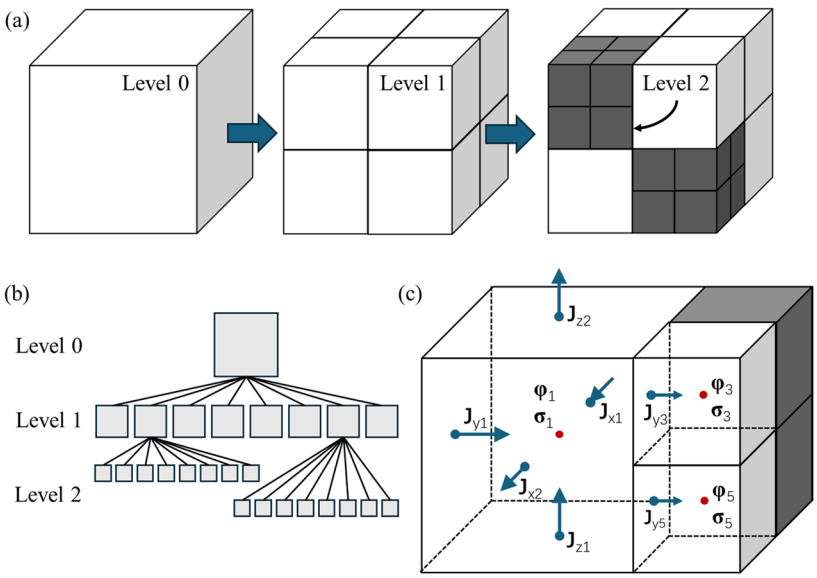

Figure 2. Illustration of octree mesh refinement for self-potential modeling. (**a**) Progression from Level 0 (uniform coarse cube) to Level 1 (basic bisection) and Level 2 (targeted local refinement around the region of interest, shown in dark gray); (**b**) Octree mesh hierarchy structure: from coarse uniform grid (top) to increasingly localized fine cells (bottom); (**c**) Schematic illustration of the octree-based finite-volume discretization. Source current densities are defined at cell faces, while electric potentials and conductivities are defined at cell centers. Note that Face-centered conductivities can be obtained by averaging adjacent cell-centered values.

The SP inverse problem seeks to recover the subsurface source current density distribution $\mathbf{J}_s$ from observed electric potential differences. Because SP data depend only on the divergence of $\mathbf{J}_s$, the inverse problem is inherently non-unique and requires regularization.

The inversion is formulated as a regularized least-squares optimization problem [29]:

$$\min_{\mathbf{m}} \Phi(\mathbf{m}) = \phi_d(\mathbf{m}) + \beta\phi_m(\mathbf{m}), \tag{5}$$

where the model vector **m** represents the discretized source current density, ϕ_d is the data misfit, ϕ_m is the model regularization term, and β controls the balance between data fitting and model smoothness.

The first term on the right-hand side of Equation (5), known as the data misfit, is defined as

$$\phi_d = \frac{1}{2} \| \mathbf{W}_d(\mathbf{d}_{\text{obs}} - \mathbf{d}_{\text{pred}}(\mathbf{m})) \|_2^2, \quad (6)$$

where $\mathbf{d}_{\text{obs}}$ are measured electric potential differences, $\mathbf{d}_{\text{pred}}$ are predicted data from the forward model, and $\mathbf{W}_d$ is a data weighting matrix derived from estimated uncertainties.

Apart from Equation (6), the second term on the right-hand side of Equation (5), which is the model regularization functional, is expressed as

$$\phi_m(\mathbf{m}) = \alpha_s \| \mathbf{m} \|_2^2 + \alpha_x \| \partial_x \mathbf{m} \|_2^2 + \alpha_y \| \partial_y \mathbf{m} \|_2^2 + \alpha_z \| \partial_z \mathbf{m} \|_2^2, \quad (7)$$

where α_s and α_x, α_y, α_z, as defined in Equation (7), control the relative weighting between the smallness and smoothness terms in the three spatial directions.

The inversion was implemented using the open-source SimPEG framework [29]. The inversion was initialized from a zero model and iterated until convergence. Predicted data were computed from the final model and compared with observations to assess the quality of the inversion.

2.2. Synthetic Test Model Setup

To validate the efficacy of the SP data inversion algorithm with octree-based discretization, a synthetic test was conducted. The primary objective was to assess the algorithm's ability to accurately recover the physical properties of a simulated SMS deposit under known conditions, before application in field SP data.

A Gaussian function was employed to simulate a raised central seafloor mound, defined mathematically as:

$$z_{\text{topo}}(x, y) = 40 \cdot \exp\left(\frac{x^2 + y^2}{80^2}\right). \quad (8)$$

The bathymetric grid was constructed using Equation (8) over a domain spanning $x, y \in [-200, 200]$ meters with a resolution of 41 × 41 nodes. To ensure appropriate boundary conditions for the potential field, a padding distance of 256 m was applied in all directions around the survey area (Figure 3).

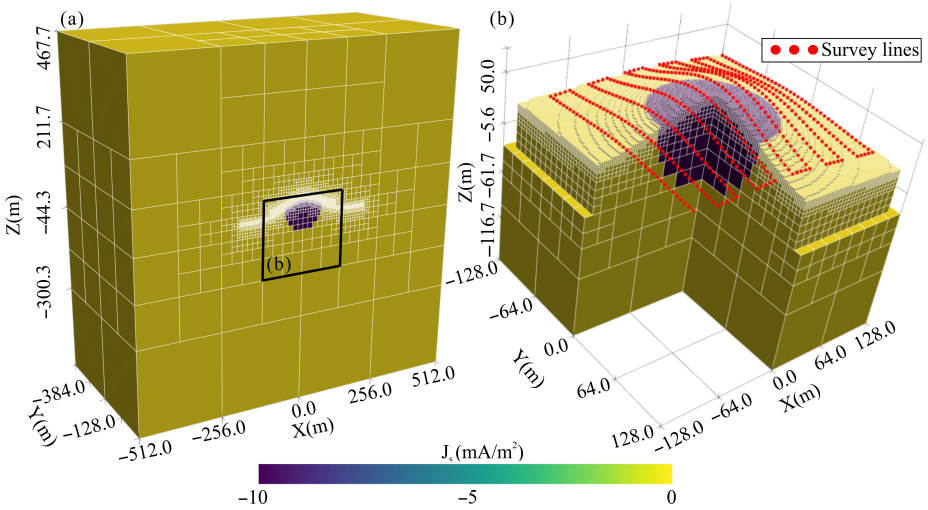

Figure 3. Synthetic 3D model current source density distribution. (**a**) Cross-section at y = 0 m showing the octree mesh discretization. The mesh is refined near the seawater-seafloor interface and along the survey lines with the smallest size of 2 m × 2 m × 2 m. The background source density is 0 A/m^3, while the mound is assigned a source density of −10 mA/m^2. (**b**) Close-up view of the model around the mound. The seawater layer (conductivity = 3.2 S/m) is not displayed, while the seabed has a background conductivity of 0.1 S/m (red dots indicate the SP survey track).

For the synthetic survey, a lawnmower-type path was simulated for an ROV. The survey covered a 200 × 200 m^2 area centered at the peak of the mound, with a line spacing of 20 m and an along-track sampling interval of 5 m. The ROV was maintained at a constant altitude of 10 m above the simulated seafloor, resulting in a total of 1681 receiver locations (Figure 3b).

A three-dimensional unstructured octree mesh was adaptively generated based on the receiver distribution and bathymetry. The mesh construction workflow consists of: (1) constructing a base mesh that covers the survey domain and receiver locations at a coarse octree level, (2) applying surface-based refinement according to the seafloor topography, with mesh resolution increasing toward the seabed to a finest cell size of 2 m and refinement restricted to the subsurface domain, and (3) performing local refinement around receiver locations to ensure forward modeling accuracy. The final mesh contained 405,259 cells. The majority of cells (317,112) were concentrated at the finest refinement level (level 9), corresponding to a minimum cell size of 2.0 m in the vicinity of the seafloor and receiver positions. Intermediate levels (levels 5–8) contained 87,499 cells, ensuring a smooth transition from fine to coarse discretization. The coarsest levels (levels 2–4) comprised only 648 cells, located mainly in the far-field and padding regions.

The seawater column was assigned a conductivity of 3.2 S/m, consistent with typical saline ocean conditions and supported by previous in situ CTD measurements in the study area [21], and was treated as inactive during inversion. In practice, the true structure beneath the seafloor is generally unknown, which is also the motivation for conducting geophysical investigations. Therefore, a homogeneous background conductivity of 0.1 S/m was assumed below the seafloor. Although this simplification may introduce smoothing or bias, it remains effective for delineating the relative distribution of anomalous sources. Synthetic SP anomalies were generated by prescribing a current source density within the target SMS body. A cylindrical-like ore body was placed at the top of the mound, with a diameter of approximately 60 m and a vertical extent of about 70 m. A current source density of -1.0×10^{-2} A/m^3 was assigned to simulate electrochemical or electrokinetic source mechanisms characteristic of sulfide mineralization. This negative source term represents a current sink, consistent with the reduced electrochemical potentials typically observed over conductive ore bodies.

2.3. Synthetic Inversion

The inversion of synthetic SP data employed a regularized least-squares optimization approach designed to recover the subseafloor source current density distribution. The data used for inversion were generated through forward modeling, with a noise level of 5% added to the synthetic responses to simulate realistic measurement errors. An L_2-norm data misfit function was used to quantify the difference between predicted and observed data. To stabilize the ill-posed inverse problem, the regularization was configured with uniform smoothing weights in all spatial directions ($\alpha_x = \alpha_y = \alpha_z = 1$) and a relatively small smallness weight ($\alpha_s = 0.01$) to prioritize structural constraints over amplitude penalization. The inversion was carried out within a gradient-based optimization framework using a Projected Gauss–Newton Conjugate Gradient (GNCG) algorithm [29]. At each iteration, the model parameters were updated by solving the linearized system using a truncated conjugate gradient solver, while bound constraints were imposed to ensure physically reasonable solutions. In addition, a beta-cooling schedule was employed to progressively balance the data misfit and regularization terms during the inversion process.

The inversion recovers a plausible distribution of current density that best fits the observed SP anomalies. As shown in Figure 4a, the model exhibits a strong negative anomaly at the center (X = 0 m, Y = 0 m) of the mound, peaking in the shallow subsurface

(Z ≈ 0 to −50 m) and decaying rapidly with depth and lateral distance, with a highest current density value of −11.5 mA/m^2, similar to the designed SP model. Figure 4b shows the fitness between the observed (blue dots) and predicted (orange dots) SP data. The predicted data closely match the observations, reproducing the oscillatory pattern with amplitudes ranging from approximately −0.10 to +0.15 mV/m. Minor discrepancies are observed at stations where the anomaly amplitude changes rapidly. These are likely attributable to the smoothing effects from regularization, but the overall fit is excellent. Figure 4c displays the inverted source current density J_s (in mA/m^2) in a vertical cross-section (YZ = 0 plane). Figure 4d illustrates the convergence of the inversion process, plotting the root-mean-square (RMS) misfit at each iteration. Starting from an initial RMS of approximately 4.0, the misfit reached a final value of 0.8 after only 5 iterations.

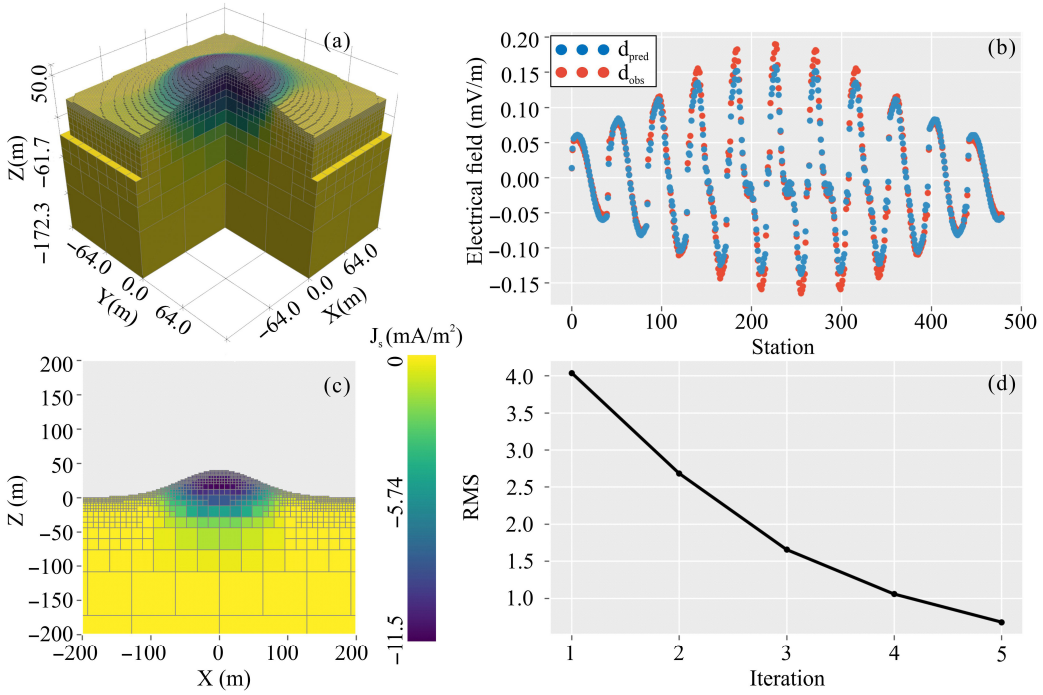

Figure 4. (**a**) Inverted 3D current density model with a highest current density of −11.5 mA/m^2; (**b**) Measured SP data (orange) obtained from forward modeling and predicted SP data (blue) from the inverted model; (**c**) Vertical cross-section of the 3D inverted current density model at Y = 0 m; (**d**) Convergence curve showing the RMS misfit versus iteration number for the synthetic SP data with 5% noise added.

The synthetic test demonstrates that the proposed inversion approach can effectively recover compact and physically reasonable source distributions with low misfit in a complex 3D setting.

2.4. Comparison with Tensor Mesh Discretization

To further evaluate the computational efficiency of the adaptive octree meshing [36], a comparison was conducted with a conventional tensor mesh using the same synthetic model described in Section 2.2 (Figure 3). For the tensor mesh, a cell size of 2 m × 2 m × 2 m was applied in regions around the seafloor, matching the finest resolution of the octree mesh (Figure 5a). The tensor mesh included padding distances of 200 m to ensure appropriate boundary conditions for forward modeling. The resulting tensor mesh contained a total of 2,846,016 cells, substantially more than the 405,259 cells in the adaptive octree mesh.

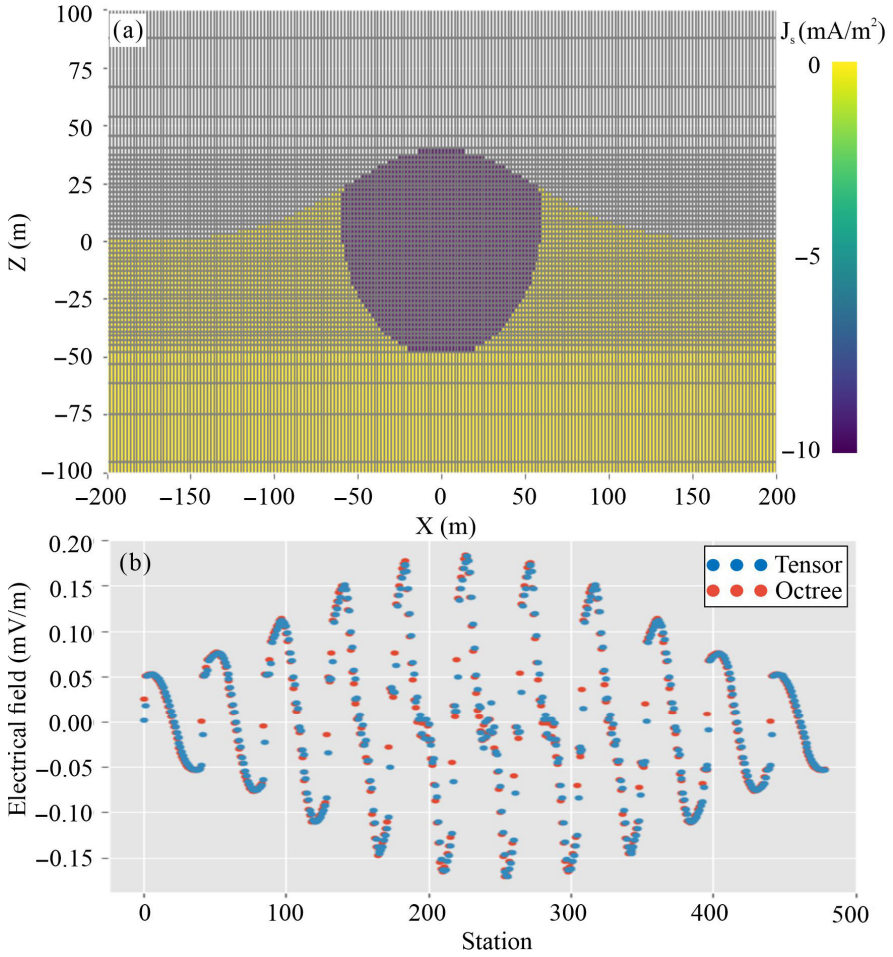

Figure 5. (**a**) Vertical cross-section of the 3D source current density model using tensor mesh; (**b**) Predicted SP data from tensor meshing (blue) and octree meshing (orange) from the inverted model.

Forward modeling was performed on both meshes under identical survey conditions and using the same computational environment. The computational time for the forward simulation was 27 min and 39 s for the tensor mesh, whereas the octree mesh required only 12 s, representing a significant reduction in computational cost. Despite the large difference in the number of cells and runtime, the forward-modeled SP responses from the octree mesh closely matched those obtained using the tensor mesh, demonstrating that the adaptive octree discretization preserves solution accuracy while greatly improving computational efficiency (Figure 5b).

This comparison illustrates the advantage of the octree approach for ROV-borne SP surveys over large and topographically complex seafloor areas. By concentrating computational resources near the seafloor and receiver locations while maintaining coarser discretization in the far-field, the method enables high-resolution inversion without prohibitive computational cost.

In the following sections, we apply this validated inversion approach to the real SP dataset acquired by ROV over the study area. We further discuss the inferred distribution of SMS deposits, which are cross-validated using independent observations, including near-bottom camera imagery and drilling data.

3. Application

3.1. Geological Background

The SP survey in this study was conducted at the Yuhuang hydrothermal field, Southwest Indian Ridge (SWIR) (Figure 1). The SWIR is an ultraslow-spreading mid-ocean ridge that has a full spreading rate of 14–16 mm/yr, and the hydrothermal activities are highly contributed by local magma supply and suitable crustal permeability [37–39]. Previous studies have shown that the total accumulation of seafloor massive sulfides in marine neovolcanic zones of the global ocean floor can reach as high as 6×10^8 t, and the accumulation of sulfides on slow- and ultraslow-spreading centers accounts for around 86% of the total tonnage of sulfide deposits at oceanic ridges [1]. The abundance of mineral resources on slow- and ultraslow-spreading ridges may be attributed to the combination of stable tectonic environment, deep hydrothermal circulation, and large-scale water-rock reactions, which facilitate the formation of large SMS deposits [37,40]. Therefore, the Yuhuang hydrothermal field located on the ultra-slow spreading SWIR shows enormous resource potential and has undergone a series of investigations since its discovery in 2010 [39,41–43].

The Yuhuang hydrothermal field (49.26°E, 37.94°S) is located near the top of the off-axis slope on the south rift wall, approximately 7–8 km from the ridge axis at a water depth of 1400–1900 m [43]. The site is likely an inactive field due to the lack of significant turbidity and temperature anomalies [39]. Through early comprehensive towing surveys, photos of SMS deposits were taken and validated using collected samples acquired from TV-grabs and drilling rigs, depicting the SMS distribution of the Yuhuang hydrothermal field [43]. Yet the surface of the YHF is typically covered by a layer of hydrothermal sediments mixed with sulfide-rich breccias, and drilling data indicate the likelihood of rich sulfides below the surface layer of calcareous sediments [42]. Current resource estimation may underestimate total reserves, as traditional seafloor surface interpretations ignore the potential contributions of deep-seated enrichment zones beneath the seabed. A SP towing operation was conducted using electrodes attached to a horizontal cable at the Yuhuang hydrothermal field, revealing a main ore body with a thickness of up to 65 m [14]. A following SP operation was also carried out in the same region using an AUV [20], identifying the same ore body along with 2 other smaller deposits. However, the towed SP survey was limited to only two lines at an altitude of approximately 50 m, and the use of a soft cable contributed to signal distortion. Although the subsequent AUV-based SP survey achieved greater coverage with multiple lines and employed electrodes mounted on rigid extension rods, the detectable SP signals were confined to an area of about 500 m × 500 m due to the relatively high survey altitude of around 100 m.

3.2. Data Acquisition and Processing

In this study, the marine SP system is mounted on the Hailong IV ROV. The 4000 m Work Class ROV, developed by Shanghai Jiao Tong University, is equipped with a seven-thruster propulsion system that provides six-degree-of-freedom motion control, a compass navigation system, an underwater hovering & patrol control system, high-definition cameras, and two manipulators. It operates at depths of up to 4000 m and provides strong maneuverability, stable hovering capability, and reliable navigation for near-bottom operations. This ROV is designed as a highly stable, powerful work platform, specifically optimized for SMS exploration, which includes geophysical survey.

The SP measurement system employed in this study utilizes non-polarizable Ag/AgCl electrodes, which are mounted on the ROV via two extension arms attached to the sides of the ROV frame (Figure 6a). Each arm has an approximate length of 1.3 m and can be extended outward using a hydraulic system integrated into the ROV. The two Ag/AgCl electrodes are securely mounted at the distal ends of the respective extension arms. This

configuration ensures that the self-potential difference is recorded along the direction of vehicle motion during survey transects. When the arms are fully extended, the electrode separation remains fixed at ~1 m, providing a consistent distance between two electrodes for detecting localized SP anomalies while the ROV navigates along pre-planned survey lines.

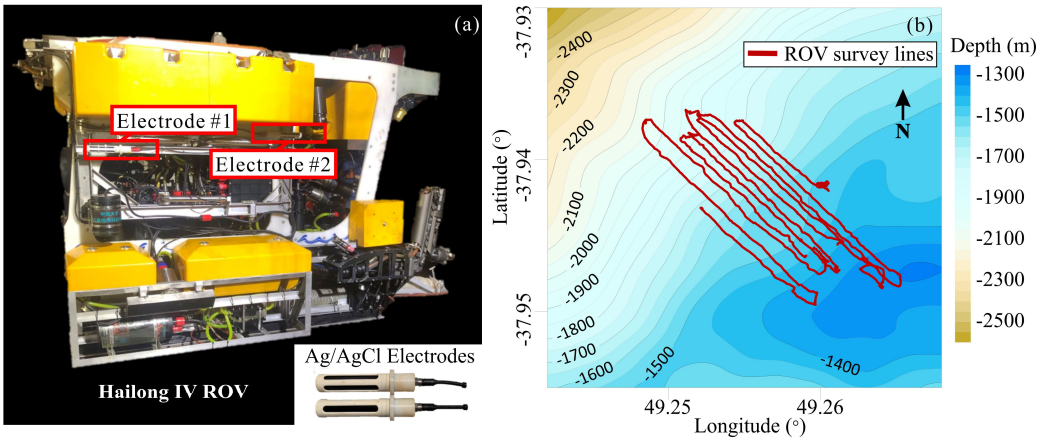

Figure 6. (**a**) The ROV-SP system applied at the Yuhuang hydrothermal field, SWIR. Non-polarizable Ag/AgCl electrodes are mounted on the ROV via two extension arms attached to the sides of the ROV frame. Each arm has an approximate length of 1.3 m and can be extended outward using a hydraulic system integrated into the ROV. When the arms are fully extended, the electrode separation remains fixed at ~1 m. (**b**) ROV tracks of the SP survey lines at the Yuhuang hydrothermal field. All 11 survey lines are along the northeast-southeast direction, covering an area of 1.072 km^2.

The ROV-SP system was deployed during the DY78 cruise in 2023. A total of 11 survey lines, covering an area of 1.072 km^2, were conducted in this study (Figure 6b). All survey lines are along the northeast-southeast direction, passing above the known Yuhuang hydrothermal field, which is known for its rich distribution of SMS after years of geological exploration.

The SP survey applied at the Yuhuang hydrothermal field includes the following steps: Firstly, the extension arms that connect the electrodes were contracted to the side of the ROV while the ROV was on the research vessel, ensuring safer deployment of the ROV into the sea. Secondly, after the ROV reached the starting point of the designated survey lines, near-bottom, continuous SP measurement was conducted while the ROV moved along the survey lines at a speed of ~0.5 kn. The topography in the study area is very complex. During the SP operation, the ROV status was monitored so that the altitude was limited to around 10 m, and the attitude variation was kept to a minimum because of the navigational control of the ROV.

The raw SP dataset comprised 5,056,425 measurement stations acquired at a sampling rate of 50 Hz. As shown in Figure 7a, although significant anomalies are present, the raw data are contaminated by high-frequency noise primarily associated with the ROV platform. The SP signal of interest represents a naturally occurring, quasi-static electric field and is therefore dominated by low-frequency components. Therefore, resampling was applied to suppress high-frequency interference while preserving the low-frequency SP signal. After resampling, the dataset was reduced to 9803 stations. The resampled data were then further processed using a second-order Savitzky–Golay filter with a window length of 21 samples to attenuate residual short-period noise while preserving the SP anomalies [44] (Figure 7b). Because the measured SP signal includes both localized anomalies and a slowly varying background correlated with water depth, environmental conditions, and long-period instrumental effects along the ROV trajectory, a background-field correction was required. To correct for the regional background field, a long-window median filter with a window

length of 1001 samples was applied to estimate the slowly varying background signal along the ROV survey lines (Figure 7b). The SP anomaly was then obtained by subtracting the estimated background field from the Savitzky–Golay–filtered signal. Finally, the processed SP data were further decimated to obtain a dataset suitable for inversion, reducing spatial redundancy in the densely sampled ROV-based measurements while improving numerical stability and computational efficiency. A total of 1234 data stations were retained for the inversion analysis (Figure 7c). A small number of stations were excluded due to abnormal ROV control parameters (heading and altitude), which could compromise data reliability.

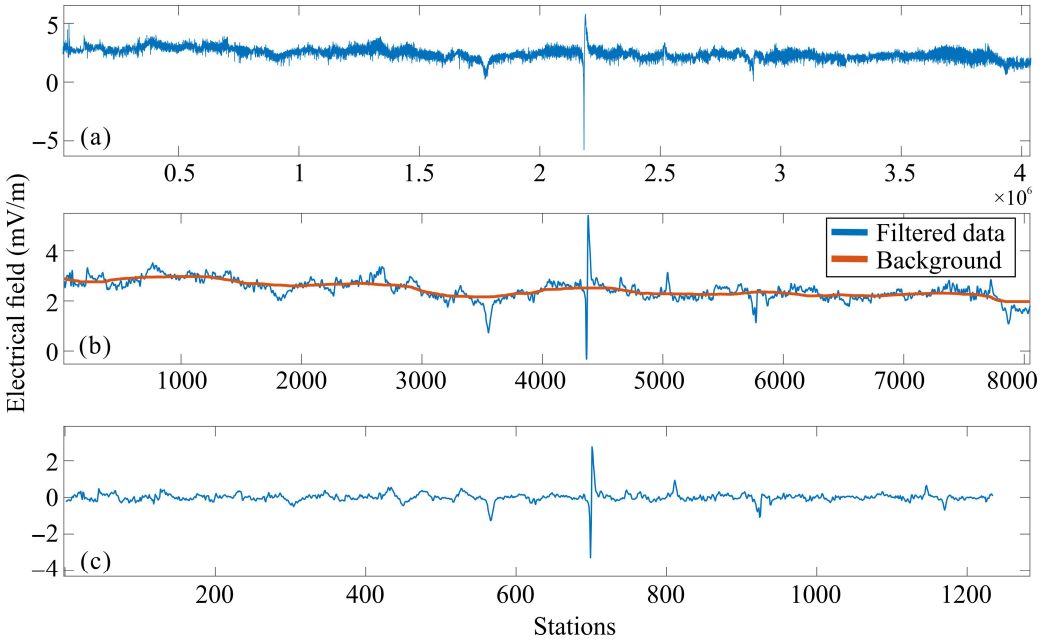

Figure 7. (**a**) Raw SP data collected using a ROV during DY78; (**b**) SP data after resampling and Savitzky–Golay filtering (blue), and a long-window median filter was used to estimate the slowly varying background field (orange) along the survey line; (**c**) Processed SP data for inversion. The processed data is defined as the difference between the filtered data and the background field.

The 3D inversion of the ROV-SP data was performed to obtain the SMS distribution at the Yuhuang hydrothermal field. Similar to the synthetic case study discussed earlier, a value of 0.1 S/m was chosen as the homogeneous conductivity of the surrounding rocks below the seafloor, and the conductivity of the seawater was set to 3.2 S/m. The inversion was carried out on a 3D octree finite-volume mesh to efficiently discretize the computational domain. The mesh consists of a total of 900,908 cells, providing a computationally efficient representation of the model space. Cell sizes range from 5 m × 5 m × 5 m in the refined regions to 1280 m × 1280 m × 1280 m in the coarsest padding parts of the domain, allowing high resolution near the seafloor and the survey lines, while maintaining coarse discretization at depth and toward the model boundaries. The inversion employs an L2-norm regularization, which promotes smooth and continuous model solutions, focusing on recovering negative anomalies associated with sulfide mineralization. The observation noise is set to be 5%, and the maximum number of iterations is 40.

4. Results

Results of the SP inversion are shown in Figure 8. The predicted SP distribution across the survey area highlights a prominent negative anomaly centered at approximately longitude 49.2588° and latitude 37.9450° (Figure 8a). This pattern is characteristic of a focused subsurface current source, consistent with electrochemical processes associated with sulfide mineralization. The anomalies align with anomalous positions observed in

the measured data. Figure 8b illustrates the comparison between the observed (orange) and predicted (blue) SP data along the survey stations. The predicted values closely match the observations, capturing the overall anomaly pattern (Figure 8c). Minor residuals occur mainly in high-amplitude regions, likely due to the use of L2-norm regularization, which enforces smoothness in the recovered model and may limit the ability to reproduce sharp variations in the data. The root mean square (RMS) decreases and stabilizes at 0.913 after 40 iterations, reflecting convergence to a stable model solution (Figure 8d).

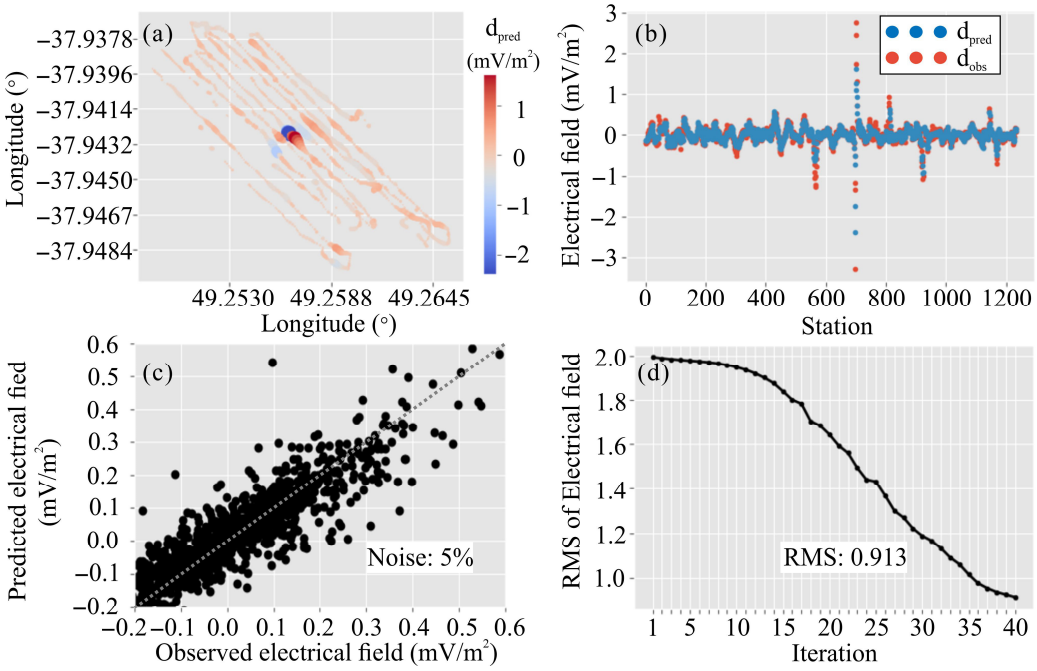

Figure 8. Results of the SP inversion at the Yuhuang hydrothermal field. (**a**) Predicted SP distribution in the survey area, with the largest negative anomaly located at approximately [49.2588, 37.9450]. (**b**) Comparison of observed (orange) and predicted (blue) SP data at each surveying station, demonstrating good fit with minor residuals. (**c**) Scatter plot of predicted versus observed SP values, with a noise level of 5% added to the data for inversion; the diagonal line indicates perfect agreement, and the points cluster closely, indicating effective recovery of the signal. (**d**) RMS of the electrical field as a function of iteration number, converging to a value of 0.913 after 40 iterations, reflecting stable model convergence.

The 3D distribution of the inverted vertical current density (Jz) obtained from the SP inversion is shown in Figure 9. The results are displayed on the finite-volume mesh and clipped to the subsurface region beneath the survey area, allowing a clear visualization of current source structures within the investigated domain. Negative Jz values, indicated by red to yellow colors, correspond to downward-directed current densities and are interpreted as zones of electrochemical activity associated with SMS mineralization.

A prominent zone of negative current density is resolved in the central part of the survey area (Zone 1, outlined by the red polygon in Figure 9). This main anomaly zone is characterized by multiple anomalies with relatively strong amplitudes and high spatial continuity, suggesting a focused region of intense current sources. The strongest negative Jz values within this zone reach amplitudes of up to approximately -0.5 mA/m^2. This pattern suggests a concentrated and well-developed current source, potentially associated with significant sulfide mineralization.

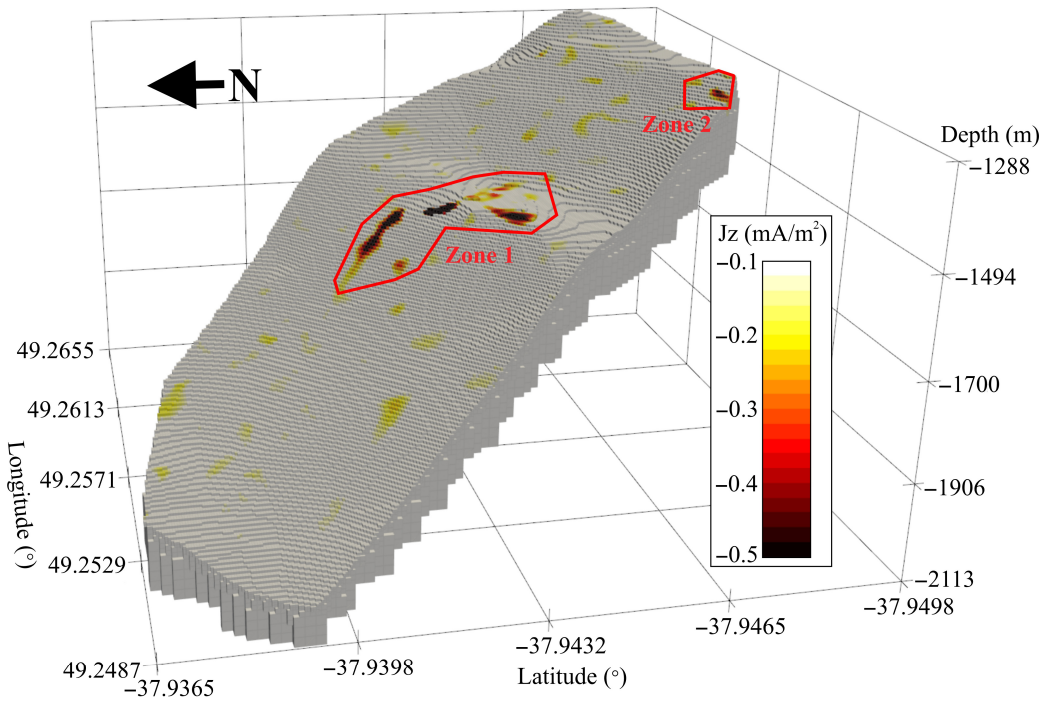

Figure 9. Inverted current density distribution (Jz in mA/m^2) derived from SP inversion, displayed on the 3D finite-volume mesh clipped to the subsurface domain below the survey area. Red to orange volumes indicate negative Jz values representing downward-directed current sources interpreted as SMS occurrences. Two distinct zones of negative current density anomalies are identified. Zone 1, located in the central part of the survey area and outlined by the red polygon, is characterized by multiple high-amplitude and laterally continuous anomalies, representing the dominant current source region. Zone 2, situated in the southern part of the survey area, exhibits smaller and weaker negative Jz anomalies, suggesting more localized or less developed current source structures. In addition, several scattered weak anomalies are observed elsewhere within the survey area.

In addition to Zone 1, a secondary zone of negative Jz anomalies is identified at the southern part of the survey area (Zone 2). Compared with Zone 1, the anomalies in Zone 2 are weaker in amplitude and smaller in spatial extent, indicating a less developed or more localized current source. This may reflect a smaller-scale or weaker mineralization system associated with reduced redox activity.

The spatial extent of zone 1 is broadly consistent with anomalous areas previously identified by towed SP and AUV-based SP surveys [13,18]. However, differences are observed in the detailed distribution of the interpreted ore bodies. Whereas Zone 2 and several surrounding weak anomalies represent additional features identified in this study that were not resolved in previous SP surveys, suggesting the potential presence of previously unrecognized mineralization in the hydrothermal field.

5. Discussion

The spatial correspondence between inverted current density anomalies and seafloor observations provides important insight into the reliability of SP inversion for delineating SMS mineralization. Within the main anomaly zone, strong negative Jz values coincide well with areas of exposed sulfide deposits identified from near-bottom camera observations, whereas regions lacking visible sulfide mineralization are mainly characterized by weak or negligible current density responses (Figure 10a). It should be noted, however, that the inverted current density represents an equivalent source distribution required to reproduce the observed SP field, rather than a direct image of the subsurface sulfide bodies. Therefore, the recovered anomalies reflect electrochemical processes and conductivity structure

associated with subsurface mineralization. Despite this limitation, the consistency between the inversion results and independent seafloor observations supports the effectiveness of the method in identifying potential mineralization zones.

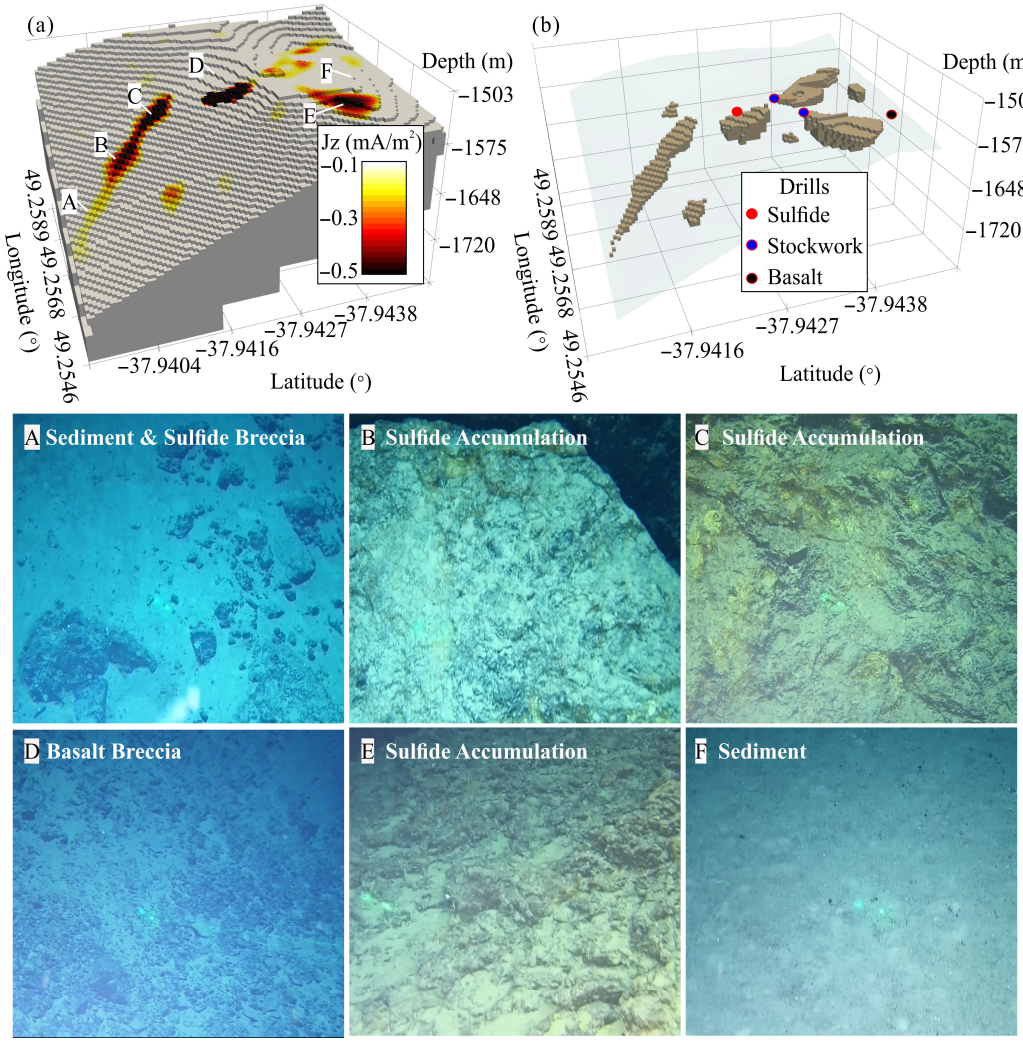

Figure 10. (**a**) Seafloor distribution of inverted vertical current density (Jz) within the main anomaly zone (zone 1). Strong negative Jz values (red to orange) correspond well with areas of exposed sulfide deposits observed in near-bottom photographs (**B**,**C**,**E**), whereas locations dominated by sediment cover or basalt breccia (**A**,**D**,**F**) exhibit weak or negligible current density responses. (**b**) Geometry of subsurface Jz anomaly bodies extracted using a threshold of $|Jz| \geq 0.15$ mA/m^2. The anomaly volumes form discrete yet spatially coherent bodies extending to a maximum depth of approximately 60 m. Drill holes intersecting massive sulfide mineralization (red) and stockwork-style sulfide mineralization (blue) are spatially associated with the anomaly bodies, while the drill hole encountering basaltic lithologies (black) is located outside the main anomaly volumes.

A more detailed comparison further highlights this relationship. Location A, characterized by sediment and sulfide breccia, corresponds to a relatively weak SP anomaly, while locations B and C, dominated by sulfide accumulations, align with strong negative Jz anomalies. In contrast, location D, featuring basalt breccia, exhibits no discernible SP anomaly. Together, anomalies at A, B, and C form an elongated, strip-like feature, suggestive of a continuous mineralization trend. Near-bottom observations at location E reveal prominent sulfide outcrops on the seafloor, which spatially correspond to a distinct SP anomaly characterized by strong Jz values. In contrast, location F, situated outside the anomaly zone, is dominated by sediment cover on the seafloor surface, resulting in negli-

gible or absent SP responses. This alignment demonstrates the efficacy of SP inversion in mapping SMS deposits through electrochemical signatures.

The three-dimensional geometry of subsurface current density anomalies extracted using a threshold of $|Jz| \geq 0.15$ mA/m^2 is shown in Figure 10b. The resulting anomaly bodies form discrete yet spatially coherent volumes that have a maximum depth of ~60 m, indicating the presence of multiple localized current source regions rather than a single continuous body. Four drill holes were completed within the main anomaly zone. Of these, three are spatially coincident with the inverted anomaly bodies, whereas the remaining drill is located outside the anomaly volumes. Among the three drill holes associated with anomaly bodies, one intersected massive sulfide mineralization (marked in red), and the other two (marked in blue) encountered stockwork-style sulfide mineralization. In contrast, the drill hole located outside the anomaly bodies intersected predominantly basaltic lithologies (marked in black).

In addition to the main anomaly zone, the spatial distribution and subsurface geometry of the inverted vertical current density within the secondary anomaly zone are illustrated in Figure 11. As shown in Figure 11a, pronounced negative Jz values are concentrated on the seafloor. Compared with the primary anomaly zone, both the spatial extent and amplitude of the Jz anomalies in this region are relatively limited, suggesting a smaller or more localized SMS distribution. Figure 11b presents the extracted subsurface geometry of the Jz anomaly bodies using a threshold of $|Jz| \geq 0.15$ mA/m^2. The resulting anomaly bodies are relatively small in volume and show limited vertical development. Most anomalies extend to a maximum subsurface depth of approximately 25 m beneath the seafloor, indicating that the inferred sulfide mineralization is shallow and lacks significant vertical continuity.

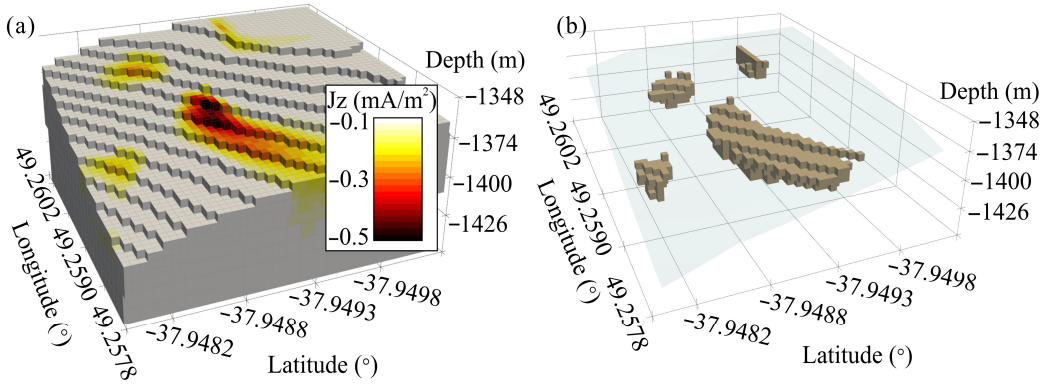

Figure 11. (**a**) Seafloor distribution of inverted vertical current density (Jz) within the secondary anomaly zone (zone 2). Strong negative Jz values (yellow to red) indicate downward-directed current sources interpreted as SMS occurrences. (**b**). Geometry of subsurface Jz anomaly bodies extracted using a threshold of $|Jz| \geq 0.15$ mA/m^2. The sulfide anomalies in this region are relatively smaller, extending to a maximum subsurface depth of approximately 25 m.

Overall, the SP inversion results, together with near-bottom observations and drilling data, confirm the geological reliability of the recovered current density anomalies. The application of the adaptive octree-based inversion to ROV-borne SP data enables high-resolution imaging of near-seafloor anomaly structures while significantly improving computational efficiency, thereby providing improved delineation of SMS mineralization. This approach demonstrates the effectiveness of combining near-bottom SP surveys with efficient discretization strategies for investigating complex seafloor environments.

6. Conclusions

This study demonstrates that near-bottom ROV-borne SP surveying and inversion, with the use of an octree-based finite-volume mesh enables efficient processing of complex seafloor topography and irregular data coverage, allowing high-resolution 3D inversion to be performed over a large survey area with manageable computational cost.

The inverted vertical current density distribution reveals a prominent anomaly zone (zone 1) spatially coincident with identified SMS occurrences, confirming the robustness of SP method for detecting sulfide-related electrochemical activity. In addition, several weaker current density anomalies are identified in surrounding areas, including a distinct secondary anomaly zone (Zone 2) that was not detected by previous surveys, highlighting the added value of high-resolution near-bottom measurements. Furthermore, the application of adaptive octree-based discretization significantly improves computational efficiency while maintaining high resolution, enabling effective inversion of large-area SP datasets in complex seafloor environments.

Despite these encouraging results, the inverted current density represents an effective source model and remains non-unique. In particular, the recovered anomaly bodies tend to appear spatially focused, which is influenced by the choice of inversion parameters, regularization strategy, and thresholding criteria. While the inverted anomalies provide robust indicators of the location and internal structure of SMS mineralization, their absolute size may slightly differ from true ore body geometry. Future work should therefore focus on integrating complementary geophysical constraints, such as EM or seismic data to better constrain anomaly geometry and scale.

Author Contributions: Conceptualization, Z.N., C.T. and Z.Z.; methodology, Z.N. and Z.Z.; software, Z.N. and Z.Z.; validation, Z.N., Z.Z. and C.T.; formal analysis, Z.N.; investigation, Z.N.; resources, C.T. and J.Z.; data curation, C.T., J.Z. and Z.N.; writing—original draft preparation, Z.N.; writing—review and editing, Z.N., Z.Z., C.T. and J.Z.; visualization, Z.N.; supervision, C.T. and J.Z.; project administration, C.T. and J.Z.; funding acquisition, C.T. and J.Z. All authors have read and agreed to the published version of the manuscript.

Funding: This research was funded by the National Natural Science Foundation of China (Grant No. 42127807 and 42276065), and the National Key Research and Development Program of China (2023YFC2811100 and 2023YFC2811101).

Data Availability Statement: Self-potential data and ROV navigation data associated with this research are available and can be obtained by contacting the corresponding author.

Acknowledgments: We extend our sincere gratitude to the captain and crew of the R/V Dayang Hao for their invaluable contributions to the success of the DY78 exploration cruise. We also deeply appreciate the support provided by the State Key Laboratory of Ocean Engineering (Shanghai Jiao Tong University). We are particularly grateful to the members of the Underwater Engineering Research Institute of Shanghai Jiao Tong University, the North Sea Bureau of the Ministry of Natural Resources, and China University of Geosciences (Beijing) for their essential contributions to ROV and SP development and application.

Conflicts of Interest: The authors declare no conflicts of interest.

Abbreviations

The following abbreviations are used in this manuscript:

ROV	Remotely Operated Vehicle
SP	Self-Potential
AUV	Autonomous Underwater Vehicle
SMS	Seafloor Massive Sulfide

SWIR	Southwest Indian Ridge
GNCG	Projected Gauss–Newton Conjugate Gradient

References

1. Hannington, M.; Jamieson, J.; Monecke, T.; Petersen, S.; Beaulieu, S. The abundance of seafloor massive sulfide deposits. *Geology* **2011**, *39*, 1155–1158. [CrossRef]
2. Hannington, M.D.; De Ronde, C.E.J.; Petersen, S. Sea-Floor Tectonics and Submarine Hydrothermal Systems. In *One Hundredth Anniversary Volume*; Hedenquist, J.W., Thompson, J.F.H., Goldfarb, R.J., Richards, J.P., Eds.; Society of Economic Geologists: Littleton, CO, USA, 2005; pp. 111–141.
3. Cherkashov, G. Seafloor Massive Sulfide Deposits: Distribution and Prospecting. In *Deep-Sea Mining: Resource Potential, Technical and Environmental Considerations*; Sharma, R., Ed.; Springer International Publishing: Cham, Switzerland, 2017; pp. 143–164.
4. Jamieson, J.W.; Gartman, A. Defining active, inactive, and extinct seafloor massive sulfide deposits. *Mar. Policy* **2020**, *117*, 103926. [CrossRef]
5. Petersen, S.; Krätschell, A.; Augustin, N.; Jamieson, J.; Hein, J.R.; Hannington, M.D. News from the seabed—Geological characteristics and resource potential of deep-sea mineral resources. *Mar. Policy* **2016**, *70*, 175–187. [CrossRef]
6. Sato, M.; Mooney, H.M. The electrochemical mechanism of sulfide self-potentials. *Geophysics* **1960**, *25*, 226–249. [CrossRef]
7. Corwin, R.F.; Hoover, D.B. The self-potential method in geothermal exploration. *Geophysics* **1979**, *44*, 226–245. [CrossRef]
8. Revil, A.; Jardani, A. *The Self-Potential Method: Theory and Applications in Environmental Geosciences*; Cambridge University Press: Cambridge, UK, 2013.
9. Revil, A.; Schwaeger, H.; Cathles, L.M., III; Manhardt, P.D. Streaming potential in porous media: 2. Theory and application to geothermal systems. *J. Geophys. Res. Solid Earth* **1999**, *104*, 20033–20048. [CrossRef]
10. Xie, J.; Cui, Y.; Liu, J.; Guo, Y.; Zhang, L.; Luo, Y.; Zhang, P. A review on theory, modeling, inversion, and application of self-potential in marine mineral exploration. *Trans. Nonferrous Met. Soc. China* **2023**, *33*, 1214–1232. [CrossRef]
11. Heinson, G.; White, A.; Constable, S.; Key, K. Marine self potential exploration*. *Explor. Geophys.* **1999**, *30*, 1–4. [CrossRef]
12. Sudarikov, S.M.; Roumiantsev, A.B. Structure of hydrothermal plumes at the Logatchev vent field, 14°45′N, Mid-Atlantic Ridge: Evidence from geochemical and geophysical data. *J. Volcanol. Geotherm. Res.* **2000**, *101*, 245–252. [CrossRef]
13. Kawada, Y.; Kasaya, T. Marine self-potential survey for exploring seafloor hydrothermal ore deposits. *Sci. Rep.* **2017**, *7*, 13552. [CrossRef] [PubMed]
14. Zhu, Z.; Tao, C.; Shen, J.; Deng, X.; Liao, S.; Zhou, J.; Wang, W.; Nie, Z.; Yu, J. Self-Potential Tomography of a Deep-Sea Polymetallic Sulfide Deposit on Southwest Indian Ridge. *J. Geophys. Res. Solid Earth* **2020**, *125*, e2020JB019738. [CrossRef]
15. Safipour, R.; Hölz, S.; Halbach, J.; Jegen, M.; Swidinsky, A. A self-potential investigation of submarine massive sulfides: Palinuro Seamount, Tyrrhenian Sea. *Geophysics* **2017**, *82*, A51–A56. [CrossRef]
16. Su, Z.; Tao, C.; Zhu, Z.; Revil, A.; Shen, J.; Nie, Z.; Li, Q.; Deng, X.; Zhou, J.; Liu, L. Joint Interpretation of Marine Self-Potential and Transient Electromagnetic Survey for Seafloor Massive Sulfide (SMS) Deposits: Application at TAG Hydrothermal Mound, Mid-Atlantic Ridge. *J. Geophys. Res. Solid Earth* **2022**, *127*, e2022JB024496. [CrossRef]
17. Zhu, Z.; Shen, J.; Tao, C.; Deng, X.; Wu, T.; Nie, Z.; Wang, W.; Su, Z. Autonomous-underwater-vehicle-based marine multicomponent self-potential method: Observation scheme and navigational correction. *Geosci. Instrum. Method. Data Syst.* **2021**, *10*, 35–43. [CrossRef]
18. Kawada, Y.; Kasaya, T. Self-potential mapping using an autonomous underwater vehicle for the Sunrise deposit, Izu-Ogasawara arc, southern Japan. *Earth Planets Space* **2018**, *70*, 142. [CrossRef]
19. Constable, S.; Kowalczyk, P.; Bloomer, S. Measuring marine self-potential using an autonomous underwater vehicle. *Geophys. J. Int.* **2018**, *215*, 49–60. [CrossRef]
20. Su, Z.; Tao, C.; Shen, J.; Revil, A.; Zhu, Z.; Deng, X.; Nie, Z.; Li, Q.; Liu, L.; Wu, T.; et al. 3D self-potential tomography of seafloor massive sulfide deposits using an autonomous underwater vehicle. *Geophysics* **2022**, *87*, B255–B267. [CrossRef]
21. Zhu, Z.; Tao, C.; Shan, Z.; Revil, A.; Su, Z.; Nie, Z.; Shen, J.; Deng, X.; Zhou, J. 3D Multicomponent Self-Potential Inversion: Theory and Application to the Exploration of Seafloor Massive Sulfide Deposits on Mid-Ocean Ridges. *Minerals* **2023**, *13*, 1098. [CrossRef]
22. Szitkar, F.; Hölz, S.; Tarits, P.; Petersen, S. Deep-Sea Electric and Magnetic Surveys Over Active and Inactive Basalt-Hosted Hydrothermal Sites of the TAG Segment (26°, MAR): An Optimal Combination for Seafloor Massive Sulfide Exploration. *J. Geophys. Res. Solid Earth* **2021**, *126*, e2021JB022082. [CrossRef]
23. MacGregor, L.; Kowalczyk, P.; Galley, C.; Weitemeyer, K.; Bloomer, S.; Phillips, N.; Proctor, A. Characterization of Seafloor Mineral Deposits Using Multiphysics Datasets Acquired from an AUV. *First Break* **2021**, *39*, 63–69. [CrossRef]
24. Kim, S.; Schankee Um, E.; Kowalczyk, P.; Kim, J.; Song, J. Marine geophysical exploration for seafloor massive sulfides using unmanned underwater vehicles. *Lead. Edge* **2025**, *44*, 901–908. [CrossRef]
25. Kasaya, T.; Iwamoto, H.; Kawada, Y. Deep-Sea DC Resistivity and Self-Potential Monitoring System for Environmental Evaluation with Hydrothermal Deposit Mining. *Front. Earth Sci.* **2021**, *9*, 608381. [CrossRef]

26. Qin, Y. Spatial distribution of spontaneous potential of metallic orebody and its application. *Geophys. Geochem. Explor.* **1985**, *9*, 268–273.
27. Revil, A.; Ehouarne, L.; Thyreault, E. Tomography of self-potential anomalies of electrochemical nature. *Geophys. Res. Lett.* **2001**, *28*, 4363–4366. [CrossRef]
28. Zhang, P.; Cui, Y.; Xie, J.; Guo, Y.; Liu, J.; Liu, J. Three-dimensional analytical solution of self-potential from regularly polarized bodies in a layered seafloor model. *Geosci. Model Dev.* **2024**, *17*, 8521–8533. [CrossRef]
29. Cockett, R.; Kang, S.; Heagy, L.J.; Pidlisecky, A.; Oldenburg, D.W. SimPEG: An open source framework for simulation and gradient based parameter estimation in geophysical applications. *Comput. Geosci.* **2015**, *85*, 142–154. [CrossRef]
30. Haber, E.; Schwarzbach, C. Parallel inversion of large-scale airborne time-domain electromagnetic data with multiple OcTree meshes. *Inverse Probl.* **2014**, *30*, 055011. [CrossRef]
31. Sill, W.R. Self-potential modeling from primary flows. *Geophysics* **1983**, *48*, 76–86. [CrossRef]
32. Hyman, J.M.; Shashkov, M. Mimetic Discretizations for Maxwell's Equations. *J. Comput. Phys.* **1999**, *151*, 881–909. [CrossRef]
33. Sheffer, M.R.; Oldenburg, D.W. Three-dimensional modelling of streaming potential. *Geophys. J. Int.* **2007**, *169*, 839–848. [CrossRef]
34. Jing, X.; Cao, H.; Zhou, J.; Liu, W.; Li, X.; Wer, Y. 3D finite-volume forward modeling of transient electromagnetic using octree meshes. *Chin. J. Geophys.* **2023**, *66*, 3524–3539. [CrossRef]
35. Haber, E.; Heldmann, S. An octree multigrid method for quasi-static Maxwell's equations with highly discontinuous coefficients. *J. Comput. Phys.* **2007**, *223*, 783–796. [CrossRef]
36. Heagy, L.J.; Cockett, R.; Kang, S.; Rosenkjaer, G.K.; Oldenburg, D.W. A framework for simulation and inversion in electromagnetics. *Comput. Geosci.* **2017**, *107*, 1–19. [CrossRef]
37. Dick, H.J.B.; Lin, J.; Schouten, H. An ultraslow-spreading class of ocean ridge. *Nature* **2003**, *426*, 405–412. [CrossRef]
38. Tao, C.; Lin, J.; Guo, S.; Chen, Y.; Wu, G.; Han, X.; German, C.; Yoerger, D.; Zhou, N.; Li, H.; et al. First active hydrothermal vents on an ultraslow-spreading center: Southwest Indian Ridge. *Geology* **2011**, *40*, 47–50. [CrossRef]
39. Tao, C.; Li, H.; Zhou, J.; Wu, T.; He, Y.; Deng, X.; Zhang, G.; Liu, W. Seafloor hydrothermal activity and polymetallic sulfide exploration on the southwest Indian ridge. *Chin. Sci. Bull.* **2014**, *59*, 2266–2276. [CrossRef]
40. German, C.R.; Petersen, S.; Hannington, M.D. Hydrothermal exploration of mid-ocean ridges: Where might the largest sulfide deposits be forming? *Chem. Geol.* **2016**, *420*, 114–126. [CrossRef]
41. Han, X.; Wu, G.; Cui, R.; Qiu, Z.; Deng, X.; Wang, Y. Discovery of a Hydrothermal Sulfide Deposit on the Southwest Indian Ridge at 49.2°E. In Proceedings of the AGU Fall Meeting 2010, Abstract #OS21C 1531, San Francisco, CA, USA, 13–17 December 2010.
42. Liao, S.; Tao, C.; Li, H.; Barriga, F.J.A.S.; Liang, J.; Yang, W.; Yu, J.; Zhu, C. Bulk geochemistry, sulfur isotope characteristics of the Yuhuang-1 hydrothermal field on the ultraslow-spreading Southwest Indian Ridge. *Ore Geol. Rev.* **2018**, *96*, 13–27. [CrossRef]
43. Yu, J.; Tao, C.; Liao, S.; Alveirinho Dias, Á.; Liang, J.; Yang, W.; Zhu, C. Resource estimation of the sulfide-rich deposits of the Yuhuang-1 hydrothermal field on the ultraslow-spreading Southwest Indian Ridge. *Ore Geol. Rev.* **2021**, *134*, 104169. [CrossRef]
44. Savitzky, A.; Golay, M.J.E. Smoothing and Differentiation of Data by Simplified Least Squares Procedures. *Anal. Chem.* **1964**, *36*, 1627–1639. [CrossRef]

Disclaimer/Publisher's Note: The statements, opinions and data contained in all publications are solely those of the individual author(s) and contributor(s) and not of MDPI and/or the editor(s). MDPI and/or the editor(s) disclaim responsibility for any injury to people or property resulting from any ideas, methods, instructions or products referred to in the content.